Responsive manipulation of neural circuit pathology by fully implantable, front-end multiplexed embedded neuroelectronics

Zifang Zhao[a,b], Claudia Cea[a], Jennifer N. Gelinas[b,c,1], and Dion Khodagholy[a,1]

[a]Department of Electrical Engineering, Columbia University, New York, NY 10027; [b]Institute for Genomic Medicine, Columbia University Irving Medical Center, New York, NY 10032; and [c]Department of Neurology, Columbia University Irving Medical Center, New York, NY 10032

Edited by John A. Rogers, Northwestern University, Evanston, IL, and approved January 25, 2021 (received for review October 29, 2020)

Responsive neurostimulation is increasingly required to probe neural circuit function and treat neuropsychiatric disorders. We introduce a multiplex-then-amplify (MTA) scheme that, in contrast to current approaches (which necessitate an equal number of amplifiers as number of channels), only requires one amplifier per multiplexer, significantly reducing the number of components and the size of electronics in multichannel acquisition systems. It also enables simultaneous stimulation of arbitrary waveforms on multiple independent channels. We validated the function of MTA by developing a fully implantable, responsive embedded system that merges the ability to acquire individual neural action potentials using conformable conducting polymer-based electrodes with real-time onboard processing, low-latency arbitrary waveform stimulation, and local data storage within a miniaturized physical footprint. We verified established responsive neurostimulation protocols and developed a network intervention to suppress pathological coupling between the hippocampus and cortex during interictal epileptiform discharges. The MTA design enables effective, self-contained, chronic neural network manipulation with translational relevance to the treatment of neuropsychiatric disease.

bioelectronics | neural interface device | closed-loop stimulation | epilepsy

Implantable bioelectronics are poised to unravel causal relationships between neural activity and brain function due to their ability to directly interact with neurons over extended periods of time (1, 2). These features also enable personalized and responsive interventions to neural network dysfunction, providing opportunities to improve treatment of neuropsychiatric disease. For a subset of patients with epilepsy, such responsive neurostimulation approaches with implanted neural interface devices are the safest and most effective treatment (3–5). To facilitate advancements in both these basic science and translational research avenues, responsive implantable electronics are required to perform three key functions to enable real-time manipulation of neural networks and affect behavior (4): 1) acquisition of high-spatiotemporal resolution neurophysiological signals (i.e., high number of simultaneously acquired channels at a sampling rate sufficient to resolve both local field potential (LFP) and action potentials of individual neurons) (6); 2) delivery of electrical stimulation to brain regions with precise localization in space and time to reduce off-target effects (7, 8) and allow causal interpretation of behavioral results (1, 9); and 3) performance of real-time neural signal processing within the implantable devices to minimize tissue extruding electronic components that increase potential risk and morbidity of implantation [such as increased chance of infection, bleeding, and problematic scar tissue formation (10)]. In addition to these functional requirements, devices should be scalable and amenable to miniaturization with the goal of lowering power consumption (5). Although a wide range of device architectures are available, none incorporate all of these features, presenting a barrier to chronic testing of neurostimulation protocols.

For instance, closed-loop electrical stimulation significantly reduces seizures in rodents with epilepsy (7, 8, 11). Such experiments require tethering of rodents because the acquisition, processing, and stimulation of neural signals has to be performed by large external electronics, restricting the scalability, duration, and translation of such interventions. Application-specific integrated circuit (ASIC) approaches can minimize the size of electronics (12–15). Current ASICs are limited to LFP bandwidth (<1,250 Hz) for closed-loop experiments, precluding acquisition of neural spiking data. Onboard field programmable gate arrays and wireless communication modules have been employed to permit cable-free experimentation, but these approaches necessitate tissue extruding head stages that can introduce surgical morbidity and limit the translational capacity. Moreover, most of these devices are designed to deliver short epochs of responsive neurostimulation, precluding evaluation of long-term effects on neural networks. Soft, battery-free devices that utilize conducting loop coils can improve the biocompatibility of implantable electronics (16–18). Battery-free devices are limited in regard to their computational capacity, though, and are often insufficient for neural data processing as such functions can require a continuous source of power. There also remains a need for low-cost responsive neurostimulation platforms that could improve accessibility for the research community without compromising functionality. Although specific neural

Significance

We introduce a multiplex-then-amplify (MTA) scheme that requires only one amplifier per multiplexer, significantly reducing the number of components in multichannel acquisition systems while enabling arbitrary waveform stimulation independently on all channels. Based on this scheme, we developed a fully implantable, miniaturized, responsive embedded system that can acquire neural oscillations and action potentials using conformable conducting polymer-based electrodes as well as perform real-time onboard processing, low-latency arbitrary waveform stimulation, and local data storage. MTA devices enabled development of a protocol for suppression of pathologic coupling within an epileptic network. These devices will allow application of targeted high-spatiotemporal resolution responsive neurostimulation approaches to a variety of brain functions, broadening our ability to chronically modify neural networks in health and disease.

Author contributions: Z.Z., J.N.G., and D.K. designed research; Z.Z., C.C., J.N.G., and D.K. performed research; Z.Z., C.C., J.N.G., and D.K. analyzed data; and Z.Z., J.N.G., and D.K. wrote the paper.

The authors declare no competing interest.

This article is a PNAS Direct Submission.

[1]To whom correspondence may be addressed. Email: jng2146@cumc.columbia.edu or dk2955@columbia.edu.

This article contains supporting information online at https://www.pnas.org/lookup/suppl/doi:10.1073/pnas.2022659118/-/DCSupplemental.

Published May 10, 2021.

network patterns have been linked to cognitive and psychiatric dysfunction, responsive neurostimulation approaches have not yet been developed to normalize this activity, in part due to these difficulties in device utilization across a variety of experimental designs.

Here, we address these challenges by developing a multiplex-then-amplify (MTA) scheme that requires only one amplifier per multiplexer, significantly reducing the size of the multichannel acquisition circuitry compared to conventional designs that necessitate one amplifier per each channel. It also enables simultaneous stimulation of arbitrary waveforms on multiple independent channels. We developed an MTA-based embedded system to establish a facile, modular interface capable of processing and storage of data within the implant and without the need for external electronics. The embedded system was integrated with a conformable, conducting polymer–based multielectrode array to yield a miniaturized, low-power, fully implantable, and responsive bioelectronic device without any extruding elements. We performed electrophysiological recording, processing, and stimulation across the hippocampal–medial prefrontal cortical (mPFC) network in freely moving rats using these conformable conducting polymer–implantable arrays. We generated automated, chronic recordings of LFP and neural spiking activity from these regions, with data stored locally within the animal. We also used the device to stimulate the hippocampal commissure and complete an automated electrical kindling procedure. These recording and stimulation capacities were integrated with an embedded processing unit to execute previously developed responsive neurostimulation protocols, including suppression of hippocampal ripples. The versatility of the device allowed us to test various protocols and develop a network intervention to suppress pathological coupling between the hippocampus and cortex generated by interictal epileptiform discharges (IEDs). Overall, these results demonstrate the effective implementation of the MTA approach within a multichannel acquisition/stimulation system to create a miniaturized, self-contained bioelectronic device for chronic neural network manipulation with translational relevance to treatment of neuropsychiatric disease.

Results

To reduce circuit size, complexity, and power consumption, we hypothesized that it would be possible to perform time-division multiplexing (MUX) on neurophysiological signals prior to amplification. This approach would require only one amplifier per multiplexer, significantly reducing the number of circuit components and the size of the device. This design would also allow direct integration of electrical stimulation circuitry into the multiplexer by bypassing the neural amplifiers (Fig. 1*A*). However, in such a setting, the electrode's electrochemical impedance becomes part of the multiplexer circuit and contributes to the input impedance, the rise time, and the switching speed of the MUX circuitry. We investigated the key circuit elements defining operation in this configuration and the range of values between which the device could accurately acquire signal when coupled with existing neural interface devices. The simplified circuit diagram of the front-end multiplexer consisted of 1) a resistor-capacitor (RC) equivalent circuit of a microelectrode accounting for the electrode–electrolyte interface capacitance (C_E) and resistance (R_E) (19, 20), and 2) a multiplexer circuit with drain parasitic capacitance (C_D), line resistance (R_M), and a switch (Fig. 1*A* and *SI Appendix*, Fig. S1*A*). In this circuit, the electrode and multiplexer capacitor are in series, and their inverse sum is the total capacitance of the circuit. The total resistance of the circuit is the sum of the electrode and line resistance; because the line resistance is substantially smaller than the electrode impedance, the total circuit resistance is dominated by the resistive component of the electrode (*SI Appendix*, Fig. S1*B*). Given these parameters, we asked over what capacitance and resistance values can this RC circuit sample neurophysiological data at spiking resolution? To resolve the waveform morphology of action potentials, a sampling rate (T_s) greater than 15 KS/s [often 20 KS/s (6, 21)] is required, corresponding to an overall multiplex switching rate of $N \times T_s$ (N = number of channels per multiplexer). With the achievable sampling rate defined as 10 times the rise time ($10 \times \tau_{RC}$) based on C_D and C_E, we found a range of values across which it would be possible to attain >20 KS/s sampling rate with at least a 16:1 microelectrode: multiplexer ratio (shaded area of Fig. 1*B*).

To validate the feasibility of this design, we fabricated a circuit containing a commercially available 16-channel multiplexer with drain capacitance within the shaded area of Fig. 1*B* (C_D = 13 pF). We utilized RC elements extracted from a 20 × 20 μm^2 conducting polymer–based electrode capable of acquiring high-quality action potentials (22–24) (*SI Appendix*, Fig. S1*B*) to define the C_E (Fig. 1*B* and *SI Appendix*, Fig. S1*C*; red star). We then evaluated the sampling performance of this multiplexer in terms of gain (output/input signal ratio), sampling rate, and uniformity across the physiological frequency spectrum and at various electrode impedances (Fig. 1 *C* and *D*). Front-end MUX was able to provide a uniform gain across physiological spectrum with 20 KS/s while maintaining a low noise floor and absent cross-talk (Fig. 1 *E* and *F* and *SI Appendix*, Fig. S1*D*), consistent with the expected values derived from the simplified circuit. The MTA design also facilitated integration of simultaneous, multichannel electrical stimulation circuitry within the acquisition circuit. Here, we bypassed the amplifier unit and utilized the multiplexer to address the desired electrodes with an arbitrary waveform generator (Fig. 1*A* and *SI Appendix*, Fig. S2). This MTA design reduced power consumption and decreased physical form factor compared to conventional MUX schemes (*SI Appendix*, Fig. S3). Overall, these results provide theoretical and experimental proof for the feasibility of front-end MUX and utilization of only one amplifier block per multiplexer for low-impedance multielectrode arrays.

Next, we designed a fully integrated MTA-based device for in vivo electrophysiological recordings in freely moving rodents (*SI Appendix*, Fig. S4). Maximal device size was determined by the volume that could be safely implanted within the dorsal subcutaneous tissue of a rat, thereby enabling cable-free mobility of the animal. The device consisted of four main functional blocks integrated into a miniaturized, fully implantable package (Fig. 2 *A* and *B*): 1) an MTA-based signal acquisition block with uniform gain and minimal cross-talk across physiological bandwidth over an extended period of time (Fig. 2*C* and *SI Appendix*, Fig. S5); 2) programmable, multiplexed stimulation amplifiers capable of delivering an arbitrary sequence of stimulation simultaneously to multiple independent channels. The stimulation pattern was generated by a digital-to-analog converter (DAC) located in the onboard embedded system (Fig. 2*D*); 3) a digital signal processing block consisting of a 32-bit microcontroller for facile real-time processing of neural data (with functions including filtering, rectification, integration, averaging, thresholding, duration detection, and generation of multiplexed stimulation patterns (Fig. 2*E*); and 4) data and power management block for local data storage (*SI Appendix*, Figs. S5*B* and S6) into a micro secure disk–based (microSD) memory unit, a low-voltage digital signaling module for real-time data transmission, and an implantable medical grade silicone–encapsulated battery equipped with a magnetic switch for external de/activation of the device (Fig. 2*F*). The MTA approach was effectively integrated with all required functional units to form a fully implantable, self-contained, responsive embedded neural electronic device.

We subsequently validated the capacity of the device to acquire high-spatiotemporal–resolution neural data when fully implanted in freely moving rats. This testing required the development of a

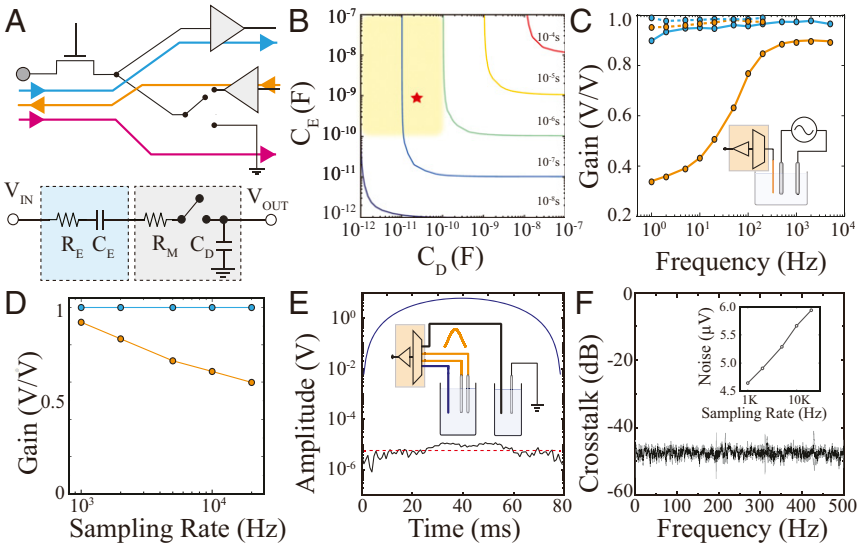

Fig. 1. MTA enables a high sampling rate, uniform gain and low-noise acquisition, as well as stimulation via neural interface devices. (*A*) Schematic highlighting the acquisition (blue), stimulation (orange), and grounding (pink) signal pathways of MTA (*Top*). A simplified circuit diagram of MTA consists of an RC model representing an electrode (cyan), and a switch with the line resistance (R_M) and drain capacitance (C_D) forming a multiplexer (gray; *Bottom*). (*B*) Temporal response of MTA under different electrode/multiplexer configurations. The colored lines indicate sampling rate defined as 10 times the rise time ($10 \times \tau_{RC}$). The yellow-shaded box shows parameters compatible with MTA design and acquisition of action potentials from neural interface devices. The red star denotes the C_D and C_E of experimental data in this work. (*C*) Frequency responses of MTA-based acquisition devices combined with high-impedance tungsten-based electrodes (100 KΩ at 1 KHz, orange) and low-impedance PEDOT:PSS-based electrodes (3 KΩ at 1 KHz, blue). The dashed and solid lines represent 1,250 Hz and 20 KHz sampling rates, respectively. *Inset*: A schematic of the experimental setup with a pair of bipolar stimulating electrodes (gray) that generate a 1 mV sweep signal (1 to 10^4 Hz) in PBS which is acquired by a microelectrode combined with MTA device (orange). (*D*) Gain versus sampling rate relationship at 100 Hz for 50 μm diameter tungsten- (orange) and PEDOT:PSS-based (blue) electrodes. (*E*) Evaluation for cross-talk during simultaneous recording and stimulation was performed using two PBS-filled chambers connected to adjacent multiplexed channels within the MTA device and a stimulating electrode delivering Gaussian stimulation (*Inset*). The recording electrode (blue) placed in the same chamber as the stimulating electrode (orange) captured the Gaussian input (blue trace), while the recording electrode associated with the adjacent MTA channel (black) placed in the second chamber remained close to the noise floor (black trace compared to red dashed line). (*F*) Absence of cross-talk across the physiologically relevant frequency spectrum. *Inset*: Root mean square noise of the MTA device with different sampling rates.

minimally invasive surgical protocol that would enable implantation of all device components in their fully assembled state (Fig. 3*A*). The front end of the device consisted of 16 linearly arranged poly(3,4-ethylenedioxythiophene) polystyrene sulfonate (PEDOT:PSS)-based electrodes embedded into a conformable parylene C shank (15 × 15 μm^2 electrodes, 20 μm spacing, 50 × 4 μm^2 shank cross-section) that could be implanted into the hippocampus using an etched tungsten microwire as a guide anchored to an etched ring at the tip of the shank (Fig. 3 *B* and *C*). A set of two conformable shanks was directly bonded to the embedded system using mixed-conducting composite particles (*SI Appendix*, Fig. S7) (25). Upon removal of the guide, the craniotomy was sealed around the conformable ribbon comprising the interconnects. Using a trocar (1 mm stainless-steel needle), silk-based suture guide line, and a small (1 to 2 mm) incision over the rat's dorsal back, we tunneled the electronics through the dorsal subcutaneous tissue. All incisions were then sutured, and the rat was allowed to recover postoperatively. In this manner, no device components extruded through the animal's skin (Fig. 3*A* and *SI Appendix*, Figs. S8 and S9).

We implanted total of 16 Long–Evans rats with these MTA devices. We acquired neural data when rats were at rest in the home cage and during active exploration of an open-field maze (Fig. 3 *D* and *E* and Movie S1). Rats were able to move freely in the absence of any external powering or tethering components, permitting facile completion of a wide range of motor behaviors required for behavioral tasks. Data quality was maintained after 1 wk of implantation, highlighting the stability of the device in a physiologic environment (Fig. 3*E*). Neurophysiologic signals should be interpretable at several different spatiotemporal scales to capture large-scale population, microcircuit synaptic, and individual cellular activity patterns. We found that MTA devices were reliable at each of these scales. Firstly, we identified characteristic broadband and low-frequency features that segregate behavioral states (Fig. 3*E*). We next detected hippocampal sharp-wave ripples, which are high-frequency (150 to 200 Hz) oscillations that display a distinctive laminar profile across layers of the CA1 hippocampal subfield. We used this profile to investigate for any cross-talk across channels, which is a key parameter in multiplexed systems. Signals will be shared across channels, invalidating analysis, if cross-talk is present. We were able to detect ripples in our MTA data using conventional algorithms (*SI Appendix*, Fig. S10*A*) and confirmed lack of cross-talk between channels by visualizing their precise spatial localization across closely spaced (50 μm) electrodes linearly embedded in an implanted probe (Fig. 3 *F* and *G* and *SI Appendix*, Fig. S10 *B* and *C*). Critically, MTA data contained high-frequency waveforms suggestive of extracellular action potential waveforms, and we were able to perform spike sorting of these waveforms into putative single units (Fig. 3*H*). Therefore, fully implanted MTA devices generate robust neurophysiological data that is suitable for all scales of computational analysis.

We next tested the devices' capacity for delivery of stimulation. Our design enabled electrical stimulation with arbitrary waveform patterns (Fig. 4*A*) and could be configured to provide either voltage or current to the tissue. We found that the onboard amplifiers provided sufficient power to drive stimulation even through high-impedance electrodes (Fig. 4*B*). Stimulation delivered to an organism in vivo must be precisely controllable. We used evoked potentials in the hippocampus to investigate

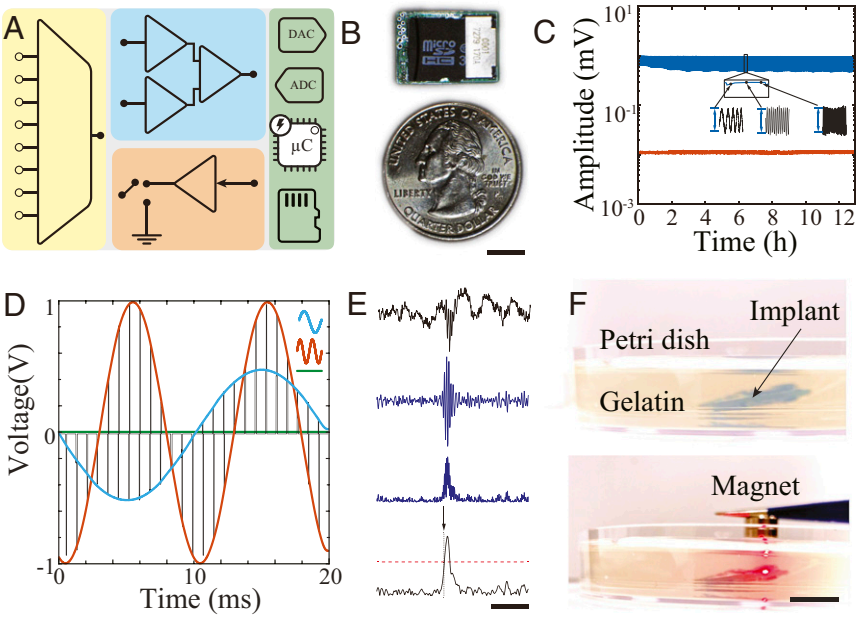

Fig. 2. MTA-based recording, stimulation, and processing within an embedded neuroelectronic system. (*A*) Simplified schematic of an MTA-based embedded system consisting of a multiplexer (yellow), acquisition amplifier (blue), stimulation unit (orange), and digital controller containing analog/digital converters, processors, and data storage unit (green). (*B*) Optical image of MTA-based embedded neuroelectronic system next to a quarter. The board dimensions are 18 × 12.8 mm^2 (Scale bar, 5 mm). (*C*) Long-term, continuous sweep signal (500 μV, 1 to 500 Hz) recording from two adjacent channels demonstrating consistent signal acquisition (blue trace) with minimum cross-talk on the adjacent channel (orange). See *SI Appendix*, Fig. S5*A* for experimental setup. (*D*) Simultaneous output voltage traces of stimulation unit delivering MTA-based multiplexed, multichannel stimulation patterns to two channels at different sine wave frequencies (orange channel = 100 Hz at 1 V; blue channel = 50 Hz at 0.5 V). Voltage of remaining channels (green trace) was unchanged. (*E*) Illustration of the real-time neural oscillation detection process. From top to bottom: 1) wideband LFP containing a ripple oscillation at the center; 2) ripple-band–filtered data; 3) rectified data; and 4) rectified trace smoothed by a moving average filter (black). The red dashed line shows 3× baseline mean value trigger level with arrow indicating the triggering onset (Scale bar, 200 ms). (*F*) Photograph of MTA device implanted in 10 mm of gelatin hydrogel to simulate implantation in tissue (*Top*). When a magnet is placed in the vicinity of the device, recording is initiated and red light-emitting diode indicator turns on (*Bottom*) (Scale bar, 10 mm).

this property in our devices. Electrical stimulation applied through the hippocampal commissure is known to evoke population synaptic activity across hippocampal layers (9, 26). The MTA device applied bipolar pulse stimuli (800 μs pulse width) to electrodes placed in the hippocampal commissure across a range of voltages. We found a consistent linear relationship between the applied voltage and evoked response amplitude, demonstrating the precision of the device's stimulation and its controllability (Fig. 4*C*). Furthermore, we could use the onboard microcontroller to program the device to give patterned stimulation at specified intervals. Rodent kindling models of epilepsy involve spaced delivery of electrical stimulation to a brain structure in order to lower the threshold for further seizure activity and generate an epileptic network. At present, most of these experimental protocols require that the animal be repeatedly connected and disconnected from the stimulation system over a period of days. We programmed our device to deliver kindling stimulation (60 Hz for 2 s, 1 ms pulse width, 50 to 100 μA) at 1 h intervals and were able to evoke regular seizure activity and kindle the animals without further experimenter intervention (Fig. 4*D* and *SI Appendix*, Fig. S11). This approach can substantially simplify various experimental protocols that necessitate regular, temporally precise delivery of electrical stimulation. In addition to these intracranial stimulation approaches, we tested the ability of the MTA device to modulate neural activity during transcranial electrical stimulation (TES). Because TES is applied to electrodes affixed to the surface of the rodent skull rather than implanted within the brain, higher voltages are required to combat attenuation by intervening tissue (8, 11, 27). MTA-delivered sinusoidal stimulation effectively and selectively entrained neural spiking, confirming the versatility of the MTA device for different neurostimulation applications (Fig. 4 *E* and *F*).

We integrated the recording and stimulation capacities of the MTA device with onboard processing to create a fully implantable responsive neurostimulation device. We first sought to execute an established neurostimulation protocol that affects memory by detecting hippocampal ripples at short latency and delivering a square pulse of electrical stimulation to the hippocampal commissure to suppress the oscillation (Fig. 5 *A* and *B*) (9, 26). The MTA's microprocessor was programmed to detect threshold crossing of the ripple band (100 to 200 Hz)–filtered power envelope (*SI Appendix*, Fig. S10*A*), and we attained a high specificity and sensitivity using offline detection as a gold standard (Fig. 5 *C*–*E* and *SI Appendix*, Fig. S10 *B* and *C*). The channel switching capacity of the device prevented amplifier saturation of recording electrodes during stimulation, enabling monitoring of neural activity shortly after stimulation. Stimulation consistently aborted the hippocampal ripple oscillations (Fig. 5*F*).

Subsequently, we aimed to leverage the arbitrary waveform stimulation capacity of the MTA device to explore the modulation of hippocampal–cortical communication. Transfer of information between hippocampus and cortex is critical for memory consolidation, and increasing temporal coupling of memory-related oscillations in the two structures improves memory (1, 28). This increased coupling has been accomplished using responsive neurostimulation protocols that detect a hippocampal ripple and trigger a cortical delta wave and spindle. Epileptic activity in the hippocampus in the form of IEDs also induces cortical delta waves and spindles (Fig. 6 *A* and *B*), but this pathologic coupling is associated with memory impairment (26, 29). Because it is unknown whether responsive neurostimulation can effectively prevent spindle generation, it has not been possible to prevent abnormal IED–spindle coupling and determine functional outcomes. We first verified that MTA-delivered

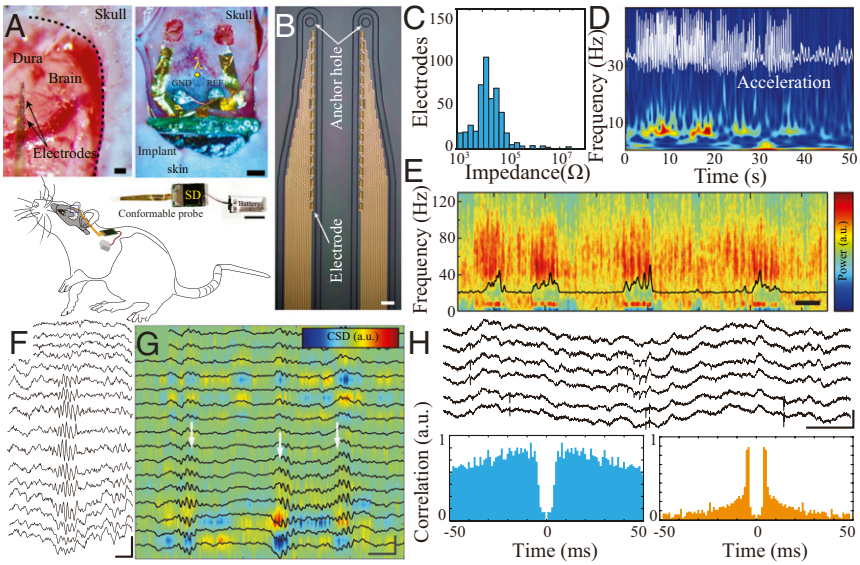

Fig. 3. MTA-based fully implantable system enables high-resolution LFP and action potential recordings in freely moving rodents. (*A*) Optical micrograph of pial surface of rat brain and conformable implantable probes prior to insertion (*Top Left* [Scale bar, 50 μm]). An optical micrograph of the MTA device partially implanted into the subcutaneous space, while conformable implantable probes are placed on top of bilateral craniotomies (*Top Right* [Scale bar, 1 mm]). Complete neural-embedded system with conformable probe and battery prior to implantation (*Middle*; note the device does not have any encapsulation for better visualization [Scale bar, 10 mm]). A simplified schematic of the overall placement and location of the implant in a rat (*Lower*). (*B*) Optical micrograph of the microfabricated conducting polymer–based electrode array (Scale bar, 20 μm). (*C*) Histogram of the impedance of the fabricated microelectrodes ($n = 480$, 4.41 ± 0.6 kΩ). (*D*) Spectrogram of hippocampal area CA1 LFP recorded during locomotion. The white superimposed trace shows the motion pattern acquired by the LFP-synchronized onboard 3-axis accelerometer. (*E*) Spectrogram of hippocampal area CA1 LFP recorded during a sleep session after 1 wk of implantation. Black trace: theta/delta band power ratio (Scale bar, 500 s). (*F*) Sample LFP traces from a linear probe illustrating the depth profile of a hippocampal ripple (Scale bar, 50 ms, 500 μV). (*G*) Current source density (CSD) and superimposed corresponding LFP traces from hippocampal area CA1 highlighting the presence of localized sources and sinks in MTA-based recordings. The white arrows indicate ripple epochs (Scale bar, 50 ms, 500 μV). (*H*) Action potentials recorded by the MTA device. Sample wide-band traces showing action potentials (*Upper*; [Scale bar, 50 ms, 500 μV]). Sample autocorrelograms of the putative single units (*Lower*).

pulse stimulation (8V, 800 μs) could evoke cortical spindles. Based on the theoretical effects of stimulation on neural activity, we then designed stimulation protocols with the goal of blocking the expression of cortical spindles. We hypothesized that the synchronized decrease in neural firing that occurs during the cortical delta wave facilitates subsequent neural recruitment to generate a spindle, such that desynchronizing stimulation would inhibit spindle expression. To test different potentially desynchronizing stimulation protocols, we implemented a real-time detection algorithm for hippocampal IEDs using the MTA (based on bandpass filtering 50 to 100 Hz and thresholding (*SI Appendix*, Fig. S12 *A* and *B*) that had similar performance compared to gold standard offline detection (Fig. 6*C*). When an IED was detected in the hippocampus, stimulation was delivered to the mPFC, and we calculated resultant cortical spindle power to determine the efficacy of the protocol in suppressing spindles. The MTA device was capable of effectively delivering a variety of stimulation protocols, including pulse trains and Gaussian waveforms. We found that a high-amplitude Gaussian wave was the only protocol that significantly decreased spindle power after a hippocampal IED (Fig. 6 *D–F* and *SI Appendix*, Figs. S12*C* and S13). Therefore, the MTA device enabled robust testing of responsive neurostimulation protocols and led to discovery of a method to modulate cortical spindle expression.

Discussion

Although the need for chronic, responsive neurostimulation devices to test hypotheses of neural network function and treat neuropsychiatric disorders is increasing, multiple limitations of this method persist. In this work, we address some of these challenges by creating a miniaturized, fully implantable device capable of storing neural data at high-spatiotemporal resolution, processing signals at minimal latency, and delivering programmable arbitrary waveform electrical stimulation. These features are enabled by a front-end MUX scheme that utilizes one amplification block per multiplexer, substantially reducing the number of amplifiers required to record multichannel data. We determined the capacitance and resistance values for which such a design could accurately sample neural data. We demonstrated that these MTA devices stably acquire high-quality in vivo neural data. We also showed accurate execution of established responsive neurostimulation protocols with MTA devices and leveraged their versatility in processing and stimulation to discover a method to suppress cortical spindle generation. Here, we used commercially available electronic components, but our design could be further improved in regard to miniaturization, power consumption, and noise parameters with dedicated ASIC design.

Furthermore, MTA devices can be adapted for use with a variety of neural interface devices. We show integration with conformable, high-density electrode arrays, minimizing the invasiveness of the implantation procedure. These devices could also be integrated with already-established neural interface devices capable of acquiring action potentials over an extended period of time (30). NeuroPace is a fully implanted responsive neurostimulation device used clinically to detect onset of seizures and deliver seizure-aborting stimulation in patients with medically refractory epilepsy. The hardware and circuit design of this device limits the sampling frequency and number of electrodes monitored. Given the importance of locating the seizure focus for successful treatment (2, 4, 31, 32), increased spatiotemporal resolution of monitoring provided by our MTA method could benefit mapping the epileptic network.

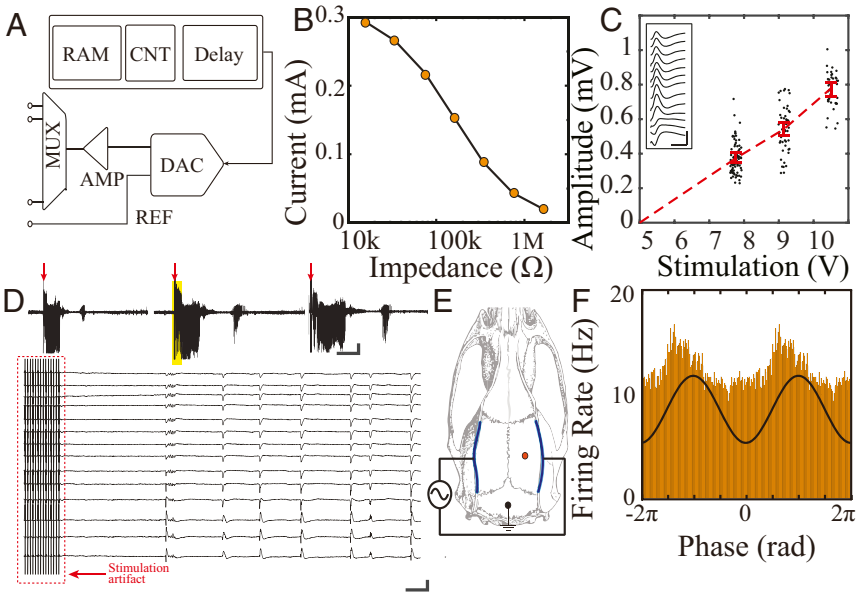

Fig. 4. MTA-based implantable system allows automatic, multimodal, controllable electrical stimulation in freely moving rodents. (*A*) Schematic of the multichannel, multiplexed stimulation block (*Top*). RAM = random access memory, CNT = counter, MUX = multiplexer, AMP = amplifier, DAC = digital analog converter, REF = reference. (*B*) Stimulation current as a function of electrode impedance, evaluated in vitro. (*C*) Hippocampal evoked-response amplitude as a function of bipolar commissure stimulation voltage. *Inset*: sample evoked-response waveform profile across CA1 layer generated by pulse stimulation (10 V, 800 μs) of the hippocampal commissure (Scale bar, 50 ms, 500 μV). (*D*) MTA system enables implementation of an automated kindling protocol. Three sample seizures automatically triggered by patterned electrical pulses delivered to the hippocampal commissure (*Upper* traces, 800 μs, 30 μA, 60 Hz for 2 s; time of stimulation noted by red arrows [Scale bar, 30 s, 500 μV]). High-resolution sample traces derived from time epoch denoted by the yellow box show stimulation artifact and onset of the ictal pattern (*Bottom* [Scale bar, 0.5 s, 1 mV]). (*E*) Schematic of transcranial electrode placement and intracranial recordings. The stimulation is delivered through the MTA system to a pair of TES electrodes. (*F*) Histogram of hippocampal multiunit activity is phase modulated by the TES stimulation (black trace).

It is increasingly appreciated that precise timing and waveform of responsive neurostimulation strongly affects the resultant neural activity patterns (7). These protocols can be tailored to increase or decrease the probability of action potential generation within a neural population (33–35). In keeping with this notion, we found that different stimulation protocols had highly variable outcomes on cortical spindle activity. Protocols that provided strong, focused bursts of current were more likely to result in spindle generation, suggesting a synchronizing effect on the corticothalamic network. In contrast, protocols that applied a current gradient over a longer duration inhibited spindle generation, possibly due to jittered action potential occurrence within the

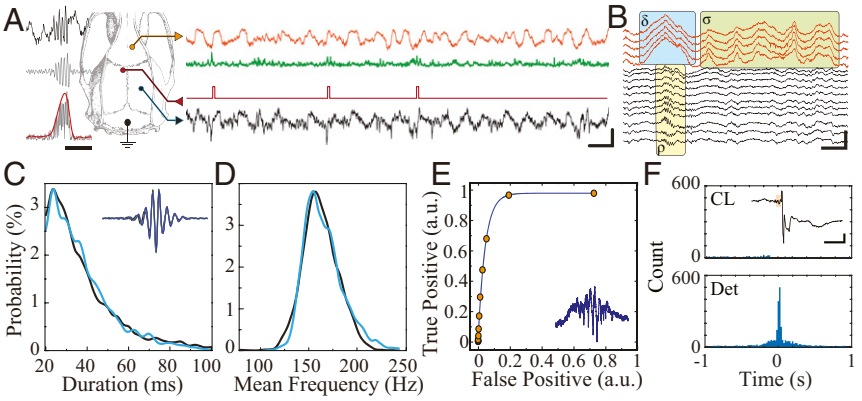

Fig. 5. MTA-based neural implant enables real-time closed-loop suppression of hippocampal ripples. (*A*) Schematic of anatomical location of recording (HC = hippocampus, blue; mPFC, orange) and stimulation electrodes for ripple suppression (*Left*). The sample raw traces from real-time simultaneous recording showing hippocampal signal (black trace), hippocampal signal processed for detection (green), and stimulation triggers (red) during NREM sleep (Scale bar, 100 ms, 500 μV). (*B*) Sample traces from MTA-device recording showing physiologic co-occurrence hippocampal ripple (ρ), cortical delta (δ), and sleep spindle (σ) with visible action potentials. (Scale bar, 100 ms, 500 μV). (*C*) Comparison of detected ripple duration obtained by the real-time closed-loop MTA-based system (blue) with offline detection of ripples obtained by conventional neural acquisition system (black) within the same animal (n = 990). (*D*) Comparison of detected ripple mean frequency obtained by the real-time closed-loop MTA-based system (blue) and offline detection of ripples obtained by conventional neural acquisition system (black) within the same animal (n = 990). (*E*) Receiver operating characteristics curve for the online ripple detector (n = 1,935). (*F*) Cross-correlogram of online detected ripples and offline detected ripples in closed-loop suppression mode (CL; n = 2,266) and detection-only mode (Det; n = 1,061). *Inset*: Sample of a closed-loop stimulation triggered by a ripple (black trace = LFP in hippocampal CA1 pyramidal layer; orange box = ripple oscillation cycles triggering detection [Scale bar, 100 ms, 200 μV]).

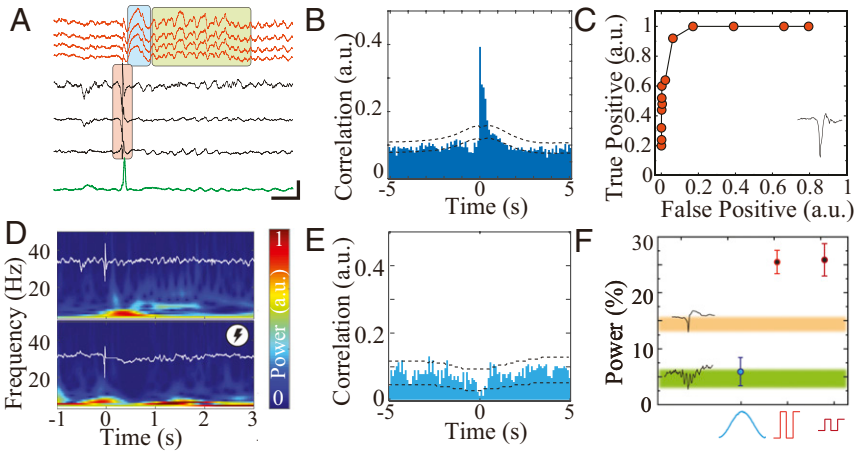

Fig. 6. Real-time, closed-loop suppression of pathological hippocampal–cortical coupling by MTA-based embedded system. (*A*) Wideband LFP showing IED (red box) in hippocampal traces (black) coupled with a delta wave (blue box) and a sleep spindle (green box) in mPFC traces (orange) during NREM sleep. The green trace is output of digital signal processor for IED detection (Scale bar, 100 ms, 500 μV). (*B*) Cross-correlogram of hippocampal IEDs and mPFC spindles. Dashed line = 95% CI (n = 4, sessions = 21, IEDs = 6,342, spindles = 6,319). (*C*) Receiver operating characteristics curve for the online IED detector compared to the offline detector (n = 1, sessions = 1, IEDs = 4,859). (*D*) Sample time-frequency spectrograms of IED-triggered responses in mPFC without closed-loop control (*Upper*) and with effective closed-loop spindle suppression protocol (*Lower*). The overlaid white traces show corresponding hippocampal LFP. (*E*) Cross-correlogram of hippocampal IEDs and mPFC spindles with Gaussian-based closed-loop spindle suppression protocol. Dashed line = 95% CI (4 animals, 21 sessions, n = 6,342). (*F*) Summary of power changes in spindle band with closed-loop Gaussian stimulation (n = 1,492 from four animals, 13 sessions, 0.059 ± 0.5), closed-loop high-amplitude pulse stimulation (n = 2,897 from four animals, six sessions, 0.26 ± 0.58), low-amplitude stimulation (n = 1,305 from four animals, six sessions, 0.26 ± 0.53). Mean and 95% CI are plotted for each group; Kolmogorov–Smirnov test P = 0.00024). The 95% CI for spindle band power after IED (orange, n = 6,342 from four animals, 21 sessions, 0.14 ± 0.51) and after ripple in nonkindled animal (green, n = 2,266 from three animals, six sessions, 0.048 ± 0.39) are plotted as color shaded areas.

population and subsequent refractoriness to synchronous LFP patterns. This ability to experiment with different stimulation parameters and assay neural response at high temporal resolution is necessary to establish more effective protocols to manipulate neural networks in specific desired directions. Low-cost devices that use off-the-shelf commercial components, such as our MTA device, have the potential to make such experimental designs more accessible to investigators. This improved access could in turn broaden the scope of neuroscientific and translational questions that could be addressed using responsive neurostimulation. Specifically, such devices allow for facile adjustment of stimulation protocols within the same animal, permitting direct comparison of network and behavioral outcomes without introducing confounders related to interanimal variability. Ongoing neuromodulation likely induces both acute and chronic network effects (36). Fully implanted responsive neuromodulation devices are optimally situated to investigate these long-term effects because they can extend the feasible duration of animal experimentation by reducing complications associated with extruding hardware (e.g., infection, bleeding, and mechanical disruption) (10).

The miniaturized footprint of the MTA device permits cable-free operation in rats, and we demonstrate integration with conformable electrode arrays and onboard storage that eliminate the need for extruding electronics. Rats can thereby participate in a wider range of tasks without being limited by cables or head caps, normalizing behavioral strategies and social interactions. Such device miniaturization also facilitates translation to human subjects by reducing the volume required for implantation (currently 60 × 27.5 × 7.5 mm within the human skull for NeuroPace). Further advances in battery design and data communication protocols will be critical for clinically relevant implementation. Although the likelihood of device failure is reduced by the absence of external components that could be disrupted by contact with the environment or damaged by animal behavior, the MTA device remains susceptible to in vivo damage. Because the electronics, cables, and batteries have a rigid structure, they are at risk for mechanical failure due to traction forces within the animal's body. Replacement of these components with conformable, stretchable materials could improve longevity despite ongoing kinetic forces associated with animal movement (22, 25, 37–39, 16, 40, 41). Furthermore, breakage of encapsulation within the body would expose device electronics to ionic fluids and jeopardize functionality. Innovation of a conformal encapsulating material that is a strong ion barrier but does not introduce substantial bulk would be highly desirable for this purpose.

Overall, the MTA approach is potentially suitable for translation to use in devices for human subjects, offering a versatile, reliable, and high-performance design for responsive bioelectronics.

Materials and Methods

Materials. PEDOT:PSS (CleviosTM PH1000) was acquired from Heraeus. Ethylene glycol, chitosan (50 to 190 kDa, 75 to 85% deacetylated), (3-Glycidyloxypropyl) trimethoxysilane (GOPS), 4-dodecyl benzene sulfonic acid, D-sorbitol (Bio-Ultra ≥99.5%), glycerol, phosphate buffered saline (PBS) tablets, poly(styrene sulfonate), and gelatin (from bovine skin) were purchased from Sigma Aldrich.

Device Fabrication and Testing. The fabrication and patterning of parylene C (Pa-C) and PEDOT:PSS-based conformable arrays have been discussed in previous publications (20, 22, 38, 42, 43). A proximity contact lithography system (Suss MA-6) was used to pattern Pa-C, Au, Pt, Ti, and PEDOT/PSS films. First, Pa-C was deposited using a chemical vapor deposition (SCS Labcoter 2) to a thickness of 1.5 μm. We used 3-(trimethoxysilyl) propyl methacrylate as an adhesion promoter and a dilute solution of industrial cleaner (Micro-90) as an antiadhesion agent. Next, the film was patterned with a 4.6 μm thick layer of AZ9260 photoresist and dry etched with a reactive-ion etching process (Oxford 80 Plus; 180 W, 50 sccm O2, 3 sccm SF6, and 2 sccm CF4 for 18 min). A lift-off process was used to pattern metal pads and interconnects. AZ nLOF 2020 (chemically amplified negative resist) was spin coated on the Pa-C film (5,500 rpm), baked at 115 °C for 60 s, exposed using Suss MA-6, and finally developed (AZ developer). With use of an e-beam metal evaporator (Angstrom at 2.10^{-6} bars), metallic layers of Ti (10 nm) and Au (150 nm) were deposited. Lift-off was performed using 1165 stripper (2 h). To enhance the conductivity of PEDOT:PSS, a mixture of PEDOT:PSS aqueous dispersion (PH-1000 from H. C. Stark) and ethylene glycol (20:5 mL ratio) was prepared and mixed with dodecylbenzenesulfonic acid (100 mL per 50 mL)

and GOPS (1 wt/vol %) to adjust surface energy and cross-link, respectively. The resulting dispersion was spin coated in two steps with a soft bake in between (120 °C, 60 s) at 650 rpm. The films were subsequently baked at 140 °C for 1 h and then immersed in deionized water to remove any excess low-molecular–weight compounds. The electrodes were characterized in vitro using PBS solution. A significantly larger Au plate compared to electrode geometry served as the reference electrode for impedance spectroscopy and measurements. The system schematics and printed circuit board (PCB) layout of the MTA system are designed in EaglePCB (Auto-Desk). Devices are assembled manually and tested with a source measure unit (B2902A, Keysight) first then programmed with a microcontroller unit programmer (ST-link).

Electrochemical Impedance. Impedance spectroscopy, modeling, and equivalent circuit extraction was done using Gamry Reference 600. Ag/AgCl and Pt wires served as reference and counter electrodes.

Electrical Characterizations. A small PCB based on 0201-series passive components and ADG1206 (Analog device) in 32-lead Lead Frame Chip Scale Package was designed and utilized to test the gain, bandwidth, noise, and rise time of MTA circuits with various electrode impedances and parasitic capacitances. A 100 mm diameter Petri dish filled with 1× PBS solution and an 18 G stainless-steel ground electrode served as the in vitro environment. PEDOT:PSS-based electrodes or 50 μm tungsten wires were bonded to the MTA board during electrical measurements. For stimulation and cross-talk measurements, a bipolar tungsten electrode was used as a stimulation electrode. Two independent PBS-filled Petri dishes served as recording and stimulation chambers to minimize any potential signal acquisition through the ground electrode.

Battery and Power Consumption. A commercially available 3.7 V, 80 mAh battery (dimensions $12 \times 30 \times 5$ mm^3) was encapsulated using implant-grade medical silicone (Nusil MED-1137) through a potting process (~1mm thickness). Although embedded electronics for acquisition, stimulation, and processing consume power, the majority of consumption occurs when data are written into the memory card (*SI Appendix*, Fig. S6). Therefore, data-writing epochs were minimized and performed in large data blocks.

Embedded System Operation Cycles. Neurophysiological signals from electrodes underwent time-division MUX prior to amplification. In this manner, only one amplifier was needed per multiplexer. However, to eliminate cross-talk and MUX parasitic charge injection, several preparatory steps and design elements were required. The MUX switch should remain open after every switch cycle to eliminate any return current due to amplifier offset currents. Even small amounts of current (1pA to 1nA) will result in a significant offset potential at the electrode due to high electrochemical impedance of microelectrodes (10 to 500 KΩ). To block MUX charge injection causing DC offsets to the high-impedance neural electrodes, a DAC (12-bit embedded within STM32F413 microcontroller or 12-bit embedded within C8051F411 microcontroller) actively counterbalanced the injected charge by delivering a preregistered sequence of pulses to the MUX drain while the drainage switch remains open. This charge delivery utilized the same circuitry as the stimulation pathway, eliminating the need for any extra components. After MUX, the signal was buffered by the first-stage operational amplifier (OPA) and filtered for antialiasing. Due to high impedance of the signal at the source, it was critical to minimize the OPA input bias current to avoid current flow into electrodes and cause saturation. The buffered and filtered signal was then differentially amplified using an instrumentation amplifier (INA) circuit. To balance the input bias current and maximally benefit from the high common-mode rejection of an INA, an identical buffering circuit was used for the reference channel. At this stage, the multiplexed and amplified signal was ready for digitization. For a short period of time after sampling (duration less than sampling cycle), the charge control switch connected the drain to the ground to clear any excess charge accumulated at the MUX's drain. During the stimulation cycle, the DAC was set to the stimulation voltage, and the MUX and the charge control switch connected the stimulation system to the selected electrode. Subsequently, the residual charge was cleared.

Animal Surgical Procedure. All animal experiments were approved by New York University Langone Medical Center and Columbia University Animal Care and Use Committees. A total of 16 freely moving Long–Evans rats had implantable probes inserted into mPFC and/or hippocampus. A bipolar stimulating electrode based on tungsten wires was implanted in the hippocampal commissure. Two miniature stainless-steel screws were fixed to the skull above the cerebellum to serve as ground and reference electrodes. Rats were kept on a regular 12 h–12 h light–dark cycle and housed in pairs before implantation but separated afterward. No prior experimentation had been performed on these rats. The animals were initially anesthetized with 2% isoflurane and maintained under anesthesia with 0.75 to 1% isoflurane during the surgery. Craniotomy was performed in three different sites (mPFC: anterior–posterior [AP] 3.5, medial–lateral [ML] −0.8, dorsal–ventral [DV] −2.4 mm; hippocampus: AP −3.5, ML 3, DV −2.0 mm; commissure: AP −0.5, ML 0.8, DV −4.2 mm). Dura mater was removed individually, and the probes were inserted to the target areas. The craniotomies were covered with gelfoam and sealed using a silicone elastomer.

Inspired by procedures used in epilepsy surgery (44), we developed a trocar-based tunneling approach using an 18-gauge stainless-steel needle to guide the MTA device through the subcutaneous tissue and allow placement without any additional incisions. A suture was used as guide line that was anchored to the device and the battery. Subsequently, the suture was removed.

Validation of Electrophysiological Recording. In vivo recordings were manually classified into wake, rapid eye movement and non-rapid eye movement (NREM) epochs based on theta/delta ratio with additional movement information extracted from the onboard accelerometer (45). Offline ripple- and spindle-detection algorithms have been described previously (29). An amplitude-threshold method was used to detect spikes from bandpass-filtered data (0.25 to 2.5 kHz) and spike waveforms were retrieved from wide-band files. Cell clustering was done by an unsupervised expectation–maximization algorithm (Klustakwik). Rats also performed free exploration of an open field maze, allowing demonstration of walking, running, and rearing behaviors during recording.

Electrical Stimulation. Stimulation could be delivered in either current or voltage mode because the DAC of the microcontroller was coupled with a noninverting operational amplifier circuit (5× gain) and an offset suppressor, enabling intrinsic output of current that could be applied directly or converted to voltage prior to application. TES occurred during sleep recording. Multiplexed stimulation voltage (40 KHz MUX speed) at 1 Hz and 1 V was delivered to TES electrodes placed bilaterally on temporal bones (11). Intracranial brain stimulation was delivered to the hippocampal commissure and mPFC during NREM sleep using bipolar electrodes (50 μm diameter tungsten–polyimide–insulated wires). The electrical stimulation was used to 1) generate hippocampal evoked responses through pulse stimulation of the hippocampal commissure, 2) induce hippocampal seizures using a kindling protocol (60 Hz bipolar 1 ms pulses delivered to the hippocampus commissure for 2 s), 3) suppress ripples during closed-loop experiments using a single 1 ms pulse delivered to the hippocampal commissure immediately after detection of a ripple, and 4) suppress hippocampal IED-induced spindles during closed-loop experiments by delivery of a variety of stimulation patterns to the mPFC. The amplitude of intracranial stimulation was derived empirically by titration of the stimulation amplitude to network effect.

Real-Time Event Detection. The closed-loop procedure was started once the rat entered NREM sleep. The data were filtered using a bandpass filter (ripples = 100 to 200 Hz, IED = 50 to 100 Hz). The first 30 s of the filtered data were used to define the noise floor of the recording in the form of SD. Subsequently, the filtered data were rectified and convolved with a moving average window leading to the instantaneous power of the signal at above-mentioned frequency bands. The instantaneous power was then compared to the noise threshold. Upon surpassing the threshold, a predefined pattern of electrical stimulation was delivered. To avoid subsequent delivery of stimulation during the period of network response, a refractory period (200 ms for ripples, 1 s for IEDs) was put in place.

Embedded System Design and Programming. Onboard microcontrollers (STMicroelectronics) coordinated neural data acquisition/stimulation and processing. Two system routines ran independently: 1) the main system service routine including the acquisition of data from analog front-end, control of stimulation patterns and timing, data transmission, and communication with the upstream data storage device and 2) the second routine performing digital signal processes including filtering, detection, averaging, and electrical stimulation parameters required for closed-loop operation. Such organization

facilitated direct loading of user-defined arbitrary waveform generation parameters through a high-level environment such as MATLAB.

Onboard Data Storage. The acquired neural data could be stored in the onboard micro-SD card. A serial peripheral interface was used to handle this operation. In addition to neural data, a 3-axis accelerometer (Freescale Semiconductor) recorded the movement of the animals. To gain high writing speed while being power efficient, data were logged in the SD card in block format. Data were subsequently retrieved and read into a personal computer in a binary file. The recording was started and stopped using an onboard magnet-triggered switch (MK24-A) that was activated by placing small permanent magnet close to the rat's body in the vicinity of the implant. Keeping the magnet in this position for 2 s or longer reset the system. To eliminate digital noise contamination originating from the memory card, a separate power regulation and ground circuit was employed. This was specifically critical when powering the system by compact implantable batteries.

Data Transfer to External Computer. We designed a C++ program that read and stored data in binary file format in a personal computer. A MATLAB monitoring program was designed to visualize the data through a graphical user interface, performing online time-frequency spectrogram calculation and signaling timing of detection and triggered stimulation for user validation.

Data Availability. All study data are included in the article and/or supporting information. All source files and experimental data are freely and publicly available at Mendeley Data repository (https://data.mendeley.com/datasets/ynb6kwh6v7/1) and at www.dion.ee.columbia.edu.

ACKNOWLEDGMENTS. This work was supported by Columbia University, School of Engineering and Applied Science, as well as by the Columbia University Irving Medical Center, Department of Neurology and Institute for Genomic Medicine. The device fabrication was performed at the Columbia Nano Initiative. This work was supported by NSF Early-concept Grants for Exploratory Research (2027135), NSF Faculty Early Career Development (CAREER) Award (1944415), and the Citizens United for Research in Epilepsy Taking Flight Award, Columbia School of Engineering. Special thanks to Dr. Gyorgy Buzsaki for his scientific support. We also thank all D.K. and J.N.G. laboratory members for their input.

1. N. Maingret, G. Girardeau, R. Todorova, M. Goutierre, M. Zugaro, Hippocampo-cortical coupling mediates memory consolidation during sleep. *Nat. Neurosci.* **19**, 959–964 (2016).
2. E. B. Geller *et al*., Brain-responsive neurostimulation in patients with medically intractable mesial temporal lobe epilepsy. *Epilepsia* **58**, 994–1004 (2017).
3. M. J. Morrell; RNS System in Epilepsy Study Group, Responsive cortical stimulation for the treatment of medically intractable partial epilepsy. *Neurology* **77**, 1295–1304 (2011).
4. E. Krook-Magnuson, J. N. Gelinas, I. Soltesz, G. Buzsáki, Neuroelectronics and biooptics: Closed-loop technologies in neurological disorders. *JAMA Neurol.* **72**, 823–829 (2015).
5. P. Jastrzebska-Perfect *et al*., Translational neuroelectronics. *Adv. Funct. Mater.* **30**, 1909165 (2020).
6. G. Buzsáki, C. A. Anastassiou, C. Koch, The origin of extracellular fields and currents—EEG, ECoG, LFP and spikes. *Nat. Rev. Neurosci.* **13**, 407–420 (2012).
7. A. Berenyi, M. Belluscio, D. Mao, G. Buzsaki, Closed-loop control of epilepsy by transcranial electrical stimulation. *Science* **337**, 735–737 (2012).
8. M. Vöröslakos *et al*., Direct effects of transcranial electric stimulation on brain circuits in rats and humans. *Nat. Commun.* **9**, 483 (2018).
9. G. Girardeau, K. Benchenane, S. I. Wiener, G. Buzsáki, M. B. Zugaro, Selective suppression of hippocampal ripples impairs spatial memory. *Nat. Neurosci.* **12**, 1222–1223 (2009).
10. J. Koch, M. Schuettler, C. Pasluosta, T. Stieglitz, Electrical connectors for neural implants: Design, state of the art and future challenges of an underestimated component. *J. Neural Eng.* **16**, 061002 (2019).
11. G. D. Spyropoulos *et al*., Transcranial electrical stimulation and recording of brain activity using freestanding plant-based conducting polymer hydrogel composites. *Adv. Mater. Technol.* **5**, 1900652 (2019).
12. A. Zhou *et al*., A wireless and artefact-free 128-channel neuromodulation device for closed-loop stimulation and recording in non-human primates. *Nat. Biomed. Eng.* **3**, 15–26 (2019).
13. J. Csicsvari *et al*., Massively parallel recording of unit and local field potentials with silicon-based electrodes. *J. Neurophysiol.* **90**, 1314–1323 (2003).
14. A. Obaid *et al*., Massively parallel microwire arrays integrated with CMOS chips for neural recording. *Sci. Adv.* **6**, eaay2789 (2020).
15. J. J. Jun *et al*., Fully integrated silicon probes for high-density recording of neural activity. *Nature* **551**, 232–236 (2017).
16. H. Zhang *et al*., Wireless, battery-free optoelectronic systems as subdermal implants for local tissue oximetry. *Sci. Adv.* **5**, eaaw0873 (2019).
17. S. S. Srinivasan, B. E. Maimon, M. Diaz, H. Song, H. M. Herr, Closed-loop functional optogenetic stimulation. *Nat. Commun.* **9**, 5303 (2018).
18. A. Burton *et al*., Wireless, battery-free subdermally implantable photometry systems for chronic recording of neural dynamics. *Proc. Natl. Acad. Sci. U.S.A.* **117**, 2835–2845 (2020).
19. D. A. Koutsouras *et al*., Impedance spectroscopy of spin-cast and electrochemically deposited PEDOT:PSS films on microfabricated electrodes with various areas. *ChemElectroChem* **4**, 2321–2327 (2017).
20. M. Sessolo *et al*., Easy-to-fabricate conducting polymer microelectrode arrays. *Adv. Mater.* **25**, 2135–2139 (2013).
21. K. D. Harris, D. A. Henze, J. Csicsvari, H. Hirase, G. Buzsáki, Accuracy of tetrode spike separation as determined by simultaneous intracellular and extracellular measurements. *J. Neurophysiol.* **84**, 401–414 (2000).
22. D. Khodagholy *et al*., NeuroGrid: Recording action potentials from the surface of the brain. *Nat. Neurosci.* **18**, 310–315 (2015).
23. M. R. Abidian, K. A. Ludwig, T. C. Marzullo, D. C. Martin, D. R. Kipke, Interfacing conducting polymer nanotubes with the central nervous system: Chronic neural recording using poly(3,4-ethylenedioxythiophene) nanotubes. *Adv. Mater.* **21**, 3764–3770 (2009).
24. M. R. Abidian, D. C. Martin, Experimental and theoretical characterization of implantable neural microelectrodes modified with conducting polymer nanotubes. *Biomaterials* **29**, 1273–1283 (2008).
25. P. Jastrzebska-Perfect *et al*., Mixed-conducting particulate composites for soft electronics. *Sci. Adv.* **6**, eaaz6767 (2020).
26. J. N. Gelinas, D. Khodagholy, T. Thesen, O. Devinsky, G. Buzsáki, Interictal epileptiform discharges induce hippocampal-cortical coupling in temporal lobe epilepsy. *Nat. Med.* **22**, 641–648 (2016).
27. N. Grossman *et al*., Noninvasive deep brain stimulation via temporally interfering electric fields. *Cell* **169**, 1029–1041.e16 (2017).
28. G. Buzsáki. Two-stage model of memory trace formation. *Neuroscience* **31**, 551–570 (1989).
29. P. Dahal *et al*., Interictal epileptiform discharges shape large-scale intercortical communication. *Brain* **142**, 3502–3513 (2019).
30. L. Luan *et al*., Ultraflexible nanoelectronic probes form reliable, glial scar-free neural integration. *Sci. Adv.* **3**, e1601966 (2017).
31. B. C. Jobst *et al*., Brain-responsive neurostimulation in patients with medically intractable seizures arising from eloquent and other neocortical areas. *Epilepsia* **58**, 1005–1014 (2017).
32. B. Lee *et al*., A single-center experience with the NeuroPace RNS system: A review of techniques and potential problems. *World Neurosurg.* **84**, 719–726 (2015).
33. Y. Cui, Z. Zhong, D. Wang, W. U. Wang, C. M. Lieber, High performance silicon nanowire field effect transistors. *Nano Lett.* **3**, 149–152 (2003).
34. Y. Takeuchi, A. Berényi, Oscillotherapeutics–Time-targeted interventions in epilepsy and beyond. *Neurosci. Res.* **152**, 87–107 (2020).
35. A. Liu *et al*., Immediate neurophysiological effects of transcranial electrical stimulation. *Nat. Commun.* **9**, 5092 (2018).
36. A. S. Hofer, M. E. Schwab, Enhancing rehabilitation and functional recovery after brain and spinal cord trauma with electrical neuromodulation. *Curr. Opin. Neurol.* **32**, 828–835 (2019).
37. C. Cea *et al*., Enhancement-mode ion-based transistor as a comprehensive interface and real-time processing unit for in vivo electrophysiology. *Nat. Mater.* **19**, 679–686 (2020).
38. G. D. Spyropoulos, J. N. Gelinas, D. Khodagholy, Internal ion-gated organic electrochemical transistor: A building block for integrated bioelectronics. *Sci. Adv.* **5**, eaau7378 (2019).
39. J. W. Jeong *et al*., Soft materials in neuroengineering for hard problems in neuroscience. *Neuron* **86**, 175–186 (2015).
40. L. Lu *et al*., Wireless optoelectronic photometers for monitoring neuronal dynamics in the deep brain. *Proc. Natl. Acad. Sci. U.S.A.* **115**, E1374–E1383 (2018).
41. D.-H. Kim, J. A. Wiler, D. J. Anderson, D. R. Kipke, D. C. Martin, Conducting polymers on hydrogel-coated neural electrode provide sensitive neural recordings in auditory cortex. *Acta Biomater.* **6**, 57–62 (2010).
42. D. Khodagholy *et al*., Highly conformable conducting polymer electrodes for in vivo recordings. *Adv. Mater.* **23**, H268–H272 (2011).
43. D. Khodagholy *et al*., Organic electronics for high-resolution electrocorticography of the human brain. *Sci. Adv.* **2**, e1601027 (2016).
44. E. Hedegärd *et al*., Complications to invasive epilepsy surgery workup with subdural and depth electrodes: A prospective population-based observational study. *J. Neurol. Neurosurg. Psychiatry* **85**, 716–720 (2014).
45. A. D. Grosmark, K. Mizuseki, E. Pastalkova, K. Diba, G. Buzsáki, REM sleep reorganizes hippocampal excitability. *Neuron* **75**, 1001–1007 (2012).